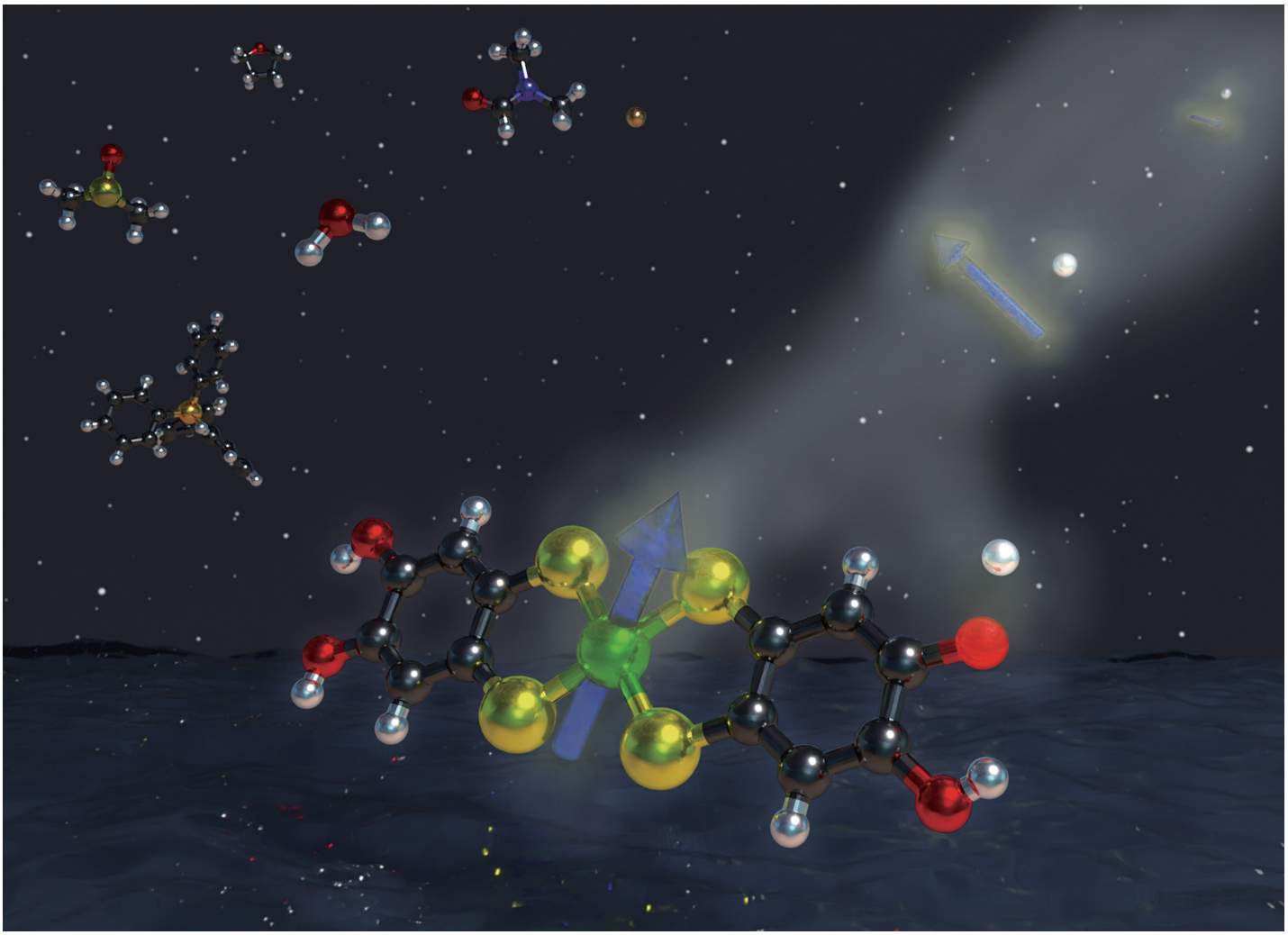

Showcasing work from The Institute for Solid State Physics, The University of Tokyo, Japan.

Modulation of the electronic states and magnetic properties of nickel catecholdithiolene complex by oxidation-coupled deprotonation

Electronic states of the nickel catecholdithiolene complex are changed with oxidation-coupled deprotonation depending on the crystallization solvents, leading to a magnetic property change of the crystals from paramagnetism to diamagnetism.

As featured in:

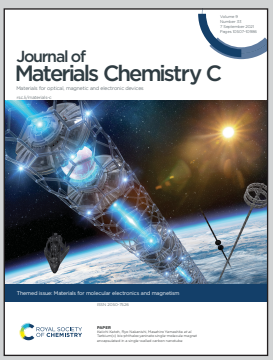

See Shun Dekura, Hatsumi Mori *et al.*, *J. Mater. Chem. C*, 2021, **9**, 10718.

ROYAL SOCIETY OF CHEMISTRY

rsc.li/materials-c

Registered charity number: 207890

Journal of Materials Chemistry C

ROYAL SOCIETY OF CHEMISTRY

PAPER

View Article Online
View Journal | View Issue

Cite this: J. Mater. Chem. C, 2021, 9, 10718

Modulation of the electronic states and magnetic properties of nickel catecholdithiolene complex by oxidation-coupled deprotonation†

So Yokomori, [a] Shun Dekura, *[a] Akira Ueda, [b] Reiji Kumai, [c] Youichi Murakami[c] and Hatsumi Mori *[a]

Electronic-state modulation utilizing the electrostatic properties and dynamics of hydrogen-bonding (H-bonding) protons is an effective strategy for realizing novel electron–proton-coupled functionalities. However, material developments based on this strategy have been limited to a few π-electron systems; thus, the realization of solid-state electron–proton-coupled functionalities is challenging. Here, we successfully synthesized new crystals based on nickel catecholdithiolene complexes, which are d/π-electron systems with H-bonds, exhibiting various deprotonation/oxidation states brought about *via* solution processes. In these crystals, unique three-dimensional framework or two-dimensional sheet structures are formed by intermolecular H-bonds between the complexes, including anionic $[O–H\cdots O]^-$ H-bonds ($d_{O\cdots O} \sim 2.59$ Å), which were advantageous for proton transfer in solid states. Importantly, detailed analyses revealed that the nickel complexes in the crystals were in various oxidation/deprotonation states. Accordingly, the magnetic properties changed from paramagnetic to non-magnetic with the oxidation of the complexes through proton-coupled electron transfer in solution processes. Density functional theory calculations revealed that the d/π electronic states of the nickel complexes in each crystal are significantly modulated depending on the deprotonation/oxidation states. We propose a possible mechanism for the oxidation-coupled deprotonation of the nickel complex, where various oxidation/deprotonation states can be obtained as crystals and controlled by recrystallization conditions, which is realized by the characteristic d/π-conjugation property and (de)protonation/redox activity of the nickel catecholdithiolene complex. The findings provide a further possibility to construct d/π-electron–proton-coupled collective functionalities based on this complex, together with significant insights for exploring novel electron–proton-coupled functionalities in the solid state.

Received 9th March 2021,
Accepted 23rd April 2021

DOI: 10.1039/d1tc01111a

rsc.li/materials-c

Introduction

Hydrogen bond (H-bond) is one of the important intermolecular interactions that control functionalities in molecular crystals.[1–9] Its strength is intermediate between the strengths of van der Waals interaction and covalent/coordination bonds; therefore, it has been widely utilized to indirectly control functionalities through structural regulation.[8,10–18] Recent studies have demonstrated that the electrostatic and dynamic properties of protons in H-bonds can directly modulate the electronic functionalities of molecular crystals in the solid state.[19–35] A clear strategy for controlling functionalities based on such electron–proton coupling is crucial to significantly expand a range of material designs for desired functionalities to pioneer novel physical properties and functionalities. However, it is still challenging to realize electron–proton coupling phenomena in the solid state.

In the past, an electron–proton-coupled state has been observed in the solid state, for example, in quinhydrone crystals consisting of a co-crystal of *p*-dihydroxybenzene (Fig. 1, left) and *p*-benzoquinone. Infrared spectroscopic observations revealed that this crystal displays a charge transfer (π-electronic state modulation) with proton transfer under high pressure.[36–38] Recently, in single-component organic conductors based on

[a] The Institute for Solid State Physics, The University of Tokyo, Kashiwa, Chiba 2778581, Japan. E-mail: s.dekura@issp.u-tokyo.ac.jp, hmori@issp.u-tokyo.ac.jp; Fax: +81 4 7136 3410; Tel: +81 4 7136 3201
[b] Department of Chemistry, Faculty of Advanced Science and Technology, Kumamoto University, 2-39-1 Kurokami, Chuo-ku, Kumamoto 860-8555, Japan
[c] Condensed Matter Research Center (CMRC) and Photon Factory, Institute of Materials Structure Science, High Energy Accelerator Research Organization (KEK), Tsukuba, Ibaraki 3050801, Japan

† Electronic supplementary information (ESI) available: Preparation, crystal structures, magnetic properties, differential Fourier map, calculation model, structures of crystals with neutral nickel complex, and ^{1}H NMR spectrum. CCDC 2065214–2065219. For ESI and crystallographic data in CIF or other electronic format see DOI: 10.1039/d1tc01111a

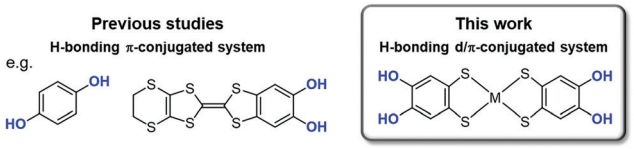

Fig. 1 Chemical structures of the H-bonding π-conjugated molecules, *p*-dihydroxybenzene and catechol-fused tetrathiafulvalene (left), and the H-bonding d/π-conjugated molecule, metal catecholdithiolene complex, [M-H_4(catdt)$_2$] (right: M is nickel in this paper).

catechol-fused tetrathiafulvalene[25–28,30–33,39,40] (Fig. 1, left) with a single-well (or low-barrier double-well for deuterated one) [O···H(D)···O] (H: hydrogen; D: deuterium) H-bond, unique electronic functionalities coupled with proton or deuteron dynamics in the solid state have been realized, such as quantum spin liquid states associated with a quantum fluctuation of protons,[26,39] and switching of magnetism and electrical conductivity.[30–33] The key to realizing such electron–proton-coupled phenomena is the significant modulation of the electronic state with H-bond formation and/or proton transfer. As noted for the aforementioned materials, the introduction of hydroxy groups to π-conjugated molecules (*e.g.*, catechol moiety) seems to be an effective molecular design based on the above-mentioned key points.[27,30,38,40,41] However, only a few crystalline materials with electron–proton-coupled functionalities have been reported to date, and most of these materials have been constructed from π-conjugated molecules, which limits the construction of the molecular design criteria and exploring of novel electron–proton-coupled functionalities. Therefore, the introduction of d electrons to π electron–proton systems is a promising strategy to address this limitation.

For this purpose, H-bonding metal dithiolene complexes functionalized with hydroxy groups are suitable candidates as the building blocks of new electron–proton-coupled materials.[42–46] Metal dithiolene complexes are d/π-electron-conjugated systems, which exhibit a wide range of electronic functionalities in solid states (magnetic/optical properties and electrical conductivity) owing to their multiple redox ability, widely delocalized frontier orbitals, and narrow HOMO–LUMO gap.[47–53] The multiple redox activity and widely delocalized frontier orbitals are advantageous for modulating their electronic state with H-bond formation and proton transfer.[35] Therefore, we expect that metal catecholdithiolene complexes, [M(catdt)$_2$],[42,44] have great potential for the further development of unique d/π-electron–proton-coupled functionalities. Previously, we successfully synthesized gold catecholdithiolene-based crystals with various unique H-bonded framework structures; however, they did not show any functionalities based on electron spin (*e.g.*, magnetic property) because of the closed-shell state of the constituent molecules.[44] In addition, there were no characteristic functionalities derived from H-bonding protons (*e.g.*, proton dynamics and proton-coupled electron transfer (PCET)).

In this study, we changed the central metal of the catechol-dithiolene complex [M(catdt)$_2$] from gold to nickel, which has one less valence d-electron than gold, and realized new crystals based on nickel catecholdithiolene complexes with different degrees of deprotonation (Fig. 1 right). In these crystals, the nickel complexes formed unique two- or three-dimensional (2D or 3D) framework structures based on multiple H-bonds. Some of them included anionic [O···H–O] H-bonds, which are advantageous for proton fluctuations in the solid state. Detailed structural analysis revealed that the deprotonated crystals underwent one-electron oxidation coupled with deprotonation *via* a solution process (*i.e.*, PCET). Accordingly, the magnetic properties change from paramagnetic to non-magnetic with oxidation-coupled deprotonation. Moreover, density functional theory (DFT) calculations demonstrated that the d/π-molecular orbitals of the nickel complexes in each crystal were significantly modulated depending on the deprotonation/oxidation states, indicating that this complex is a suitable building block for the realization of proton–electron-coupled functionalities in the solid state.

Results and discussion

Molecular structures and arrangements

Nickel catecholdithiolene complex (Ph_4P)$_3$[Ni-H_4(catdt)$_2$]Br_2, **2-Ni** (Ph_4P: tetraphenylphosphonium), as in a previous study,[42] was obtained. Subsequently, **2-Ni** and the green powder prepared from **2-Ni** were recrystallized under several conditions (see the Experimental section) to produce new crystals: (Ph_4P)[Ni-H_4(catdt)$_2$]·DMSO, **3-Ni-4H·DMSO**; (Ph_4P)[Ni-H_3(catdt)$_2$]·0.5H_2O, **3-Ni-3H·0.5H_2O**; (Ph_4P)[Ni-H_3(catdt)$_2$]·0.5THF, **3-Ni-3H·0.5THF**; and (Ph_4P)$_2$[Ni-H_2(catdt)$_2$]·2H_2O, **3-Ni-2H·H_2O** (THF: tetrahydrofuran, DMSO: dimethyl sulfoxide). The compositions and structures of the crystals were determined by single-crystal X-ray structural analysis. The crystallographic data for the **3-Ni-4H·DMSO**, **3-Ni-3H·0.5THF**, **3-Ni-3H·0.5H_2O**, and **3-Ni-2H·2H_2O** crystals are summarized in Table S1 and Fig. S1 (ESI†).

Non-deprotonated Ni complex crystal: 3-Ni-4H·DMSO

The crystal structure of the DMSO-containing crystal **3-Ni-4H·DMSO** is shown in Fig. 2 and Fig. S2 and S3 (ESI†). The asymmetric unit consisted of one Ph_4P^+ cation, two half nickel complexes, and one molecule of DMSO; the nickel complex was deduced to be monoanionic. In this crystal, a 3D framework structure (Fig. 2a and Fig. S2, ESI†) based on 1D H-bonded zigzag chains was constructed based on multiple [O–H···O] H-bonds between the nickel complexes and those between the nickel complex and DMSO molecule (Fig. 2b and Fig. S3, ESI†). Owing to the construction of the 3D framework encapsulating the bulky cations, there was no significant orbital interaction between the nickel complexes. The construction of such a 3D framework based on the metal dithiolene complex has been limited to a few examples of crystals consisting of a gold catecholdithiolene complex in our previous work[44] and metal iodothiazoledithiolene complexes.[54] With regard to the molecular structures of the nickel complex in this crystal, the C–O and C–S bond lengths are almost the same as those of the Ni complex in **2-Ni** and the [Au(catdt)$_2$]$^-$ complex[44] (Table 1). This indicates that the hydroxy groups of the nickel complex in this crystal are not

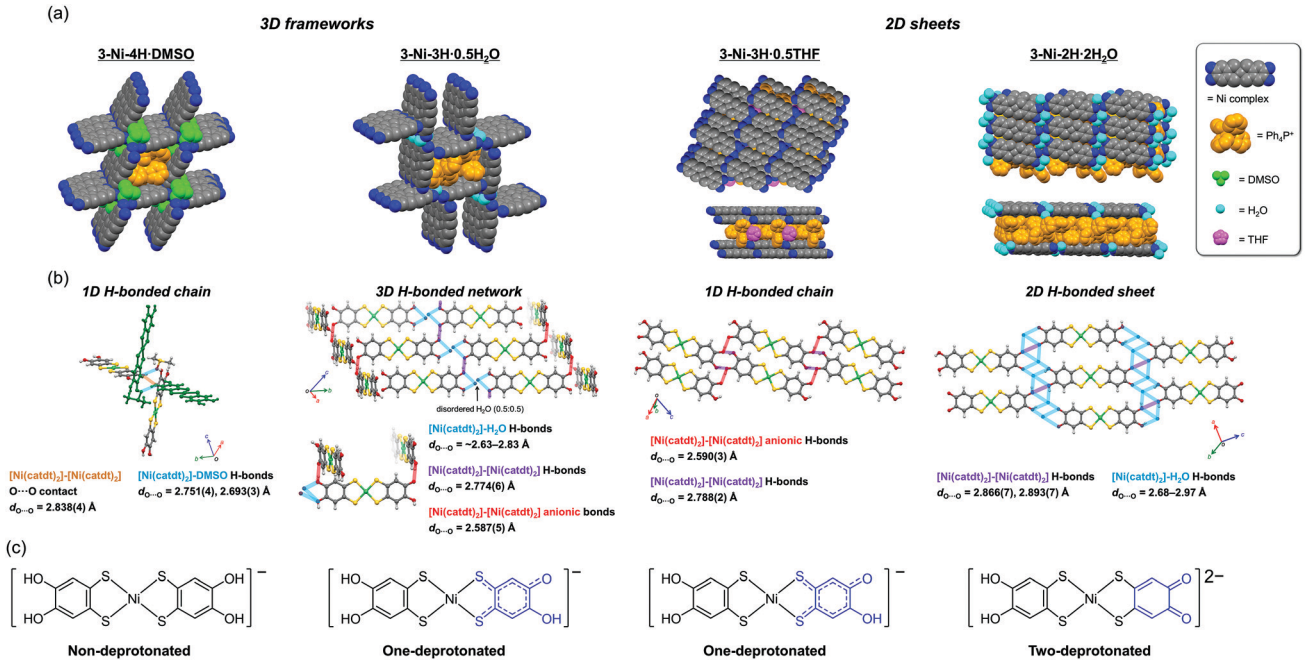

Fig. 2 (a) Assembled structures, (b) H-bond network structures, and (c) molecular structures of the nickel complexes of **3-Ni-4H·DMSO**, **3-Ni-3H·0.5H$_2$O**, **3-Ni-3H·0.5THF**, and **3-Ni-2H·2H$_2$O** (from left to right). Blue and purple dashed lines indicate the anionic [O···H–O]$^-$ H-bonds and common [O···H–O] H-bonds between the nickel complexes, respectively. Orange and light-blue dashed lines show the [O···O] short contacts between nickel complexes and [O···H–O] H-bonds between the nickel complex and crystal solvents, respectively (light green = Ni, yellow = S, gray = C, red = O, and white = H in(b)).

deprotonated (Fig. 1 and 2c). Based on this fact and the monoanionic state of the nickel complex, the complex in this crystal is determined to be a radical species (S = 1/2).

One-deprotonated Ni complex crystals: 3-Ni-3H·0.5H$_2$O and 3-Ni-3H·0.5THF

The compositions of **3-Ni-3H·0.5H$_2$O** and **3-Ni-3H·0.5THF** were determined to be $(Ph_4P)[Ni\text{-}H_3(catdt)_2]\cdot 0.5H_2O$ and $(Ph_4P)[Ni\text{-}H_3(catdt)_2]\cdot 0.5THF$, respectively, by X-ray structural analysis. This indicates that the nickel complexes were in a monoanionic state in both crystals. **3-Ni-3H·0.5H$_2$O** is isostructural to the previously reported $(Ph_4P)[Au(catdt)_2]\cdot 0.5H_2O$;[44] the complexes are connected by multiple [O–H···O] H-bonds to form a 3D framework structure (Fig. 2 and Fig. S4, ESI†). In **3-Ni-3H·0.5THF**, the nickel complexes formed a 2D sheet structure, where Ph_4P^+ and THF molecules were sandwiched between the 2D sheets (Fig. 2a and Fig. S5, S6, ESI†). The sheet was constructed from 1D H-bonded chains formed by [O–H···O] H-bonds between the nickel complexes ($d_{O\cdots O}$ = 2.788(2) Å and 2.590(3) Å, Fig. 2b and Fig. S6, ESI†). The crystal solvent molecule, THF, has no H-bonds with the nickel complex.

The molecular structures of the nickel complexes in these crystals were different from those in **3-Ni-4H·DMSO** and previously reported $[Au(catdt)_2]^-$ complex crystals.[44] Although all the four C–O bond lengths of the $[Au(catdt)_2]^-$ complex and the nickel complex in **3-Ni-4H·DMSO** were almost the same, one or two of the four C–O bonds of the nickel complexes in **3-Ni-3H·0.5H$_2$O** and **3-Ni-3H·0.5THF** were significantly shorter (d_c = 1.297(7) Å for **3-Ni-3H·0.5H$_2$O**, and d_a = 1.327(2) Å and d_d = 1.323(2) Å for **3-Ni-3H·0.5THF**; Table 1, Fig. S7 and S8, ESI†); their lengths are intermediate between the lengths of single-bond C–O (~1.37 Å, *cf.* non-deprotonated **3-Ni-4H·DMSO**) and double-bond C=O (~1.23 Å, *cf.* nickel *o*-benzoquinonedithiolene complex[42]). These results indicate that these hydroxy groups with

Table 1 Molecular structures of $[Ni\text{-}H_4(catdt)_2]$ complexes with bond labels and the C–S and C–O bond lengths (in Å) of the nickel dithiolene complexes of **3-Ni-4H·DMSO**, **3-Ni-3H·0.5H$_2$O**, **3-Ni-3H·0.5THF**, and **3-Ni-2H·2H$_2$O**. Entries shown in bold show relatively short C–O bond lengths

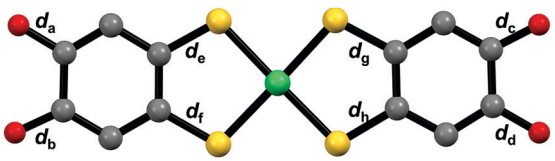

3-Ni-4H·DMSO				
C–O bonds	d_a = 1.373(5)	d_b = 1.369(4)	d_c = 1.362(3)	d_d = 1.369(4)
C–S bonds	d_e = 1.742(3)	d_f = 1.734(3)	d_g = 1.737(3)	d_h = 1.746(3)
3-Ni-3H·0.5H$_2$O				
C–O bonds	d_a = 1.358(7)	d_b = 1.373(7)	**d_c = 1.297(7)**	d_d = 1.347(7)
C–S bonds	d_e = 1.732(5)	d_f = 1.740(6)	d_g = 1.725(6)	d_h = 1.708(5)
3-Ni-3H·0.5THF				
C–O bonds	**d_a = 1.327(2)**	d_b = 1.357(3)	d_c = 1.359(3)	**d_d = 1.323(2)**
C–S bonds	d_e = 1.736(2)	d_f = 1.714(2)	d_g = 1.727(2)	d_h = 1.721(2)
3-Ni-2H·2H$_2$O				
C–O bonds	**d_a = 1.291(8)**	**d_b = 1.30(1)**	d_c = 1.35(1)	d_d = 1.364(9)
C–S bonds	d_e = 1.763(7)	d_f = 1.688(8)	d_g = 1.781(7)	d_h = 1.674(8)

short C–O bond lengths are deprotonated, and the C–O bond has a double-bond character and a semiquinone-like structure (Fig. 2c and Fig. S7, S8, ESI†). Here, the existence of one short C–O bond per nickel complex in **3-Ni-3H·0.5H$_2$O** indicates that the nickel complex is singly deprotonated. In contrast, in **3-Ni-3H·0.5THF**, the C–O bonds of the two hydroxy groups were short. The C–O bonds of these two hydroxy groups are slightly longer than those in **3-Ni-3H·0.5H$_2$O** (1.327(2) Å and 1.323(2) Å *vs.* 1.297(7) Å) and these two hydroxy groups formed anionic $[O–H\cdots O]^-$ H-bonds with each other ($d_{O\cdots O}$ = 2.590(3) Å; Fig. 2b); therefore, one deprotonation occurred for the two hydroxy groups (Fig. 2c and Fig. S7, S8, ESI†). Namely, the nickel complex in **3-Ni-3H·0.5THF** is also in a one-deprotonated state. Considering the one-deprotonation and mono-anionic state of the nickel complex, one-electron oxidation coupled with deprotonation of the complex occurred in these crystals.

Two-deprotonated Ni complex crystal: 3-Ni-2H·2H$_2$O

Crystals of **3-Ni-2H·2H$_2$O** were obtained together with **3-Ni-4H·DMSO** and **3-Ni-3H·0.5H$_2$O** crystals under the same recrystallization conditions (DMSO/H$_2$O). Although the nickel complexes in **3-Ni-4H·DMSO**, **3-Ni-3H·0.5H$_2$O**, and **3-Ni-3H·0.5THF** were monoanionic, **3-Ni-2H·2H$_2$O** contained a Ph_4P^+ cation and nickel complex in the ratio of 2 : 1 (formula: $(Ph_4P)_2[Ni\text{-}H_2(catdt)_2]\cdot 2H_2O$) determined by X-ray structural analysis; the nickel complex is dianion. This crystal has a 2D H-bonded sheet structure based on a nickel complex similar to that of **3-Ni-3H·0.5THF** (Fig. 2a and Fig. S9, ESI†). However, the 2D sheet in this crystal consisted of the nickel complexes and water molecules with multiple $[O–H\cdots O]$ H-bonds ($d_{O\cdots O}$ = 2.68–2.97 Å, Fig. 2b) in contrast to **3-Ni-3H·0.5THF**, where the nickel complexes solely formed the 2D H-bonded sheets. Although this crystal has two equivalents of bulky cation molecules to the nickel complex, a 2D H-bonded sheet structure was constructed because of a small water molecule with proton-accepting and -donating abilities that help to form multiple $[O–H\cdots O]$ H-bonds that connect the nickel complexes.

The C–O bond lengths of the nickel complex also show different features from those of **3-Ni-3H·0.5H$_2$O** and **3-Ni-3H·0.5THF**. In this crystal, the C–O bonds of the two hydroxy groups belonging to the same ligand in the nickel complex were short (d_a = 1.291(8) Å and d_b = 1.30(1) Å, Table 1 and Fig. S10, ESI†). Considering that the short C–O bond lengths are almost the same as those of the nickel complex in **3-Ni-3H·0.5H$_2$O**, both hydroxy groups are deprotonated. Thus, the two-deprotonation occurred for the complex in this crystal, which, together with the dianion state of the complex, suggests that one-electron oxidation of the complex occurred as is the case with the one-deprotonated nickel complex crystals.

Summarizing the results of X-ray structural analyses, we successfully synthesized nickel-catecholdithiolene-based crystals with peculiar H-bonded structures (2D sheets or 3D frameworks), where nickel complexes in the obtained crystals have different degrees of deprotonation (non-, one-, or two-deprotonated state). In other words, we controlled the degree of deprotonation in catecholdithiolene-based crystals by changing the crystallization conditions.

Change in magnetic properties with deprotonation

As discussed above, considering the number of protons on the catechol ligands and the charge of the nickel complexes in these crystals, deprotonation-coupled oxidation occurred in the crystals **3-Ni-3H·0.5H$_2$O**, **3-Ni-3H·0.5THF**, and **3-Ni-2H·2H$_2$O** through PCET in solution processes. The monoanionic and neutral nickel dithiolene complexes are generally in open-shell (S = 1/2)[12,52,55–57] and closed-shell (S = 0)[45,57–59] states, respectively, and the former assemblies exhibit magnetic properties based on electron spins. The non-deprotonated crystal **3-Ni-4H·DMSO** is thus expected to be in an open-shell state (S = 1/2). In contrast, the nickel complexes in both the one-deprotonated crystals (**3-Ni-3H·0.5H$_2$O** and **3-Ni-3H·0.5THF**) and the two-deprotonated crystal (**3-Ni-2H·2H$_2$O**) involving one-electron oxidation are expected to be in a closed-shell state (S = 0). Such differences in the electronic configuration should be reflected in their electronic properties, such as their magnetic properties.

To investigate the electronic (oxidation) states of the nickel complexes and magnetic properties in each crystal, electron spin resonance (ESR) measurements for these crystals, as well as the magnetic susceptibility measurement for **3-Ni-4H·DMSO**, were performed. As expected, the non-deprotonated complex crystal, **3-Ni-4H·DMSO**, showed an ESR signal at approximately 3260–3310 G at room temperature (Fig. 3 and Fig. S11a, ESI†). The g value was estimated to be 2.039–2.068 from Lorentzian fitting analysis (Fig. S11b and c, ESI†). This value is consistent with the values of reported nickel dithiolene complexes,[42] and thus this ESR signal is attributed to the electron spins on the nickel complexes. Furthermore, the temperature dependence of the magnetic susceptibility of **3-Ni-4H·DMSO** obeys the Curie–Weiss law with very weak antiferromagnetic interaction (Curie temperature T_C = −0.148 K, Fig. S12, ESI†). This result is consistent with the absence of significant π–π interactions between the nickel complexes in the 3D framework structure (Fig. 2a and Fig. S2, ESI†). In contrast, other deprotonated complex crystals (**3-Ni-3H·0.5H$_2$O**, **3-Ni-3H·0.5THF**, and **3-Ni-2H·2H$_2$O**) showed no ESR signals (Fig. 3), which revealed

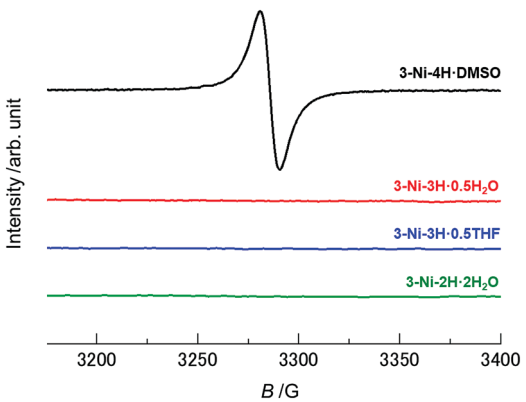

Fig. 3 ESR spectra of **3-Ni-4H·DMSO**, **3-Ni-3H·0.5H$_2$O**, **3-Ni-3H·0.5THF**, and **3-Ni-2H·2H$_2$O**. The black, red, blue, and green solid lines indicate the spectra of **3-Ni-4H·DMSO**, **3-Ni-3H·0.5H$_2$O**, **3-Ni-3H·0.5THF**, and **3-Ni-2H·2H$_2$O**, respectively. The ESR signals derived from the electron spins were not observed in the crystals except for **3-Ni-4H·DMSO**.

that the nickel complexes in these crystals were in closed-shell states. These results are consistent with the degrees of deprotonation indicated by X-ray structural analyses; the nickel complex is singly deprotonated in **3-Ni-3H·0.5H$_2$O** and **3-Ni-3H·0.5THF** and is doubly deprotonated in **3-Ni-2H·2H$_2$O**. Thus, we successfully controlled the magnetic properties of these nickel dithiolene complex crystals from paramagnetic to non-magnetic utilizing multiple deprotonation and oxidation (*i.e.*, PCET) in solution processes.

Electronic-state modulation with oxidation-coupled deprotonation

DFT calculations based on the experimentally obtained structure of each crystal revealed the significant influence of oxidation-coupled deprotonation on the d/π electronic states of the nickel complexes (Fig. 4). The singly-occupied molecular orbital (SOMO) and the lowest unoccupied molecular orbital (LUMO) of **3-Ni-4H·DMSO** were similar to the highest occupied molecular orbital (HOMO) and LUMO of the monoanionic gold catechol-dithiolene complex reported in our previous paper.[44] The HOMOs and LUMOs of the deprotonated complex crystals correspond to the SOMO−1 and SOMO of the non-deprotonated crystal **3-Ni-4H·DMSO**, respectively, because of the one-electron oxidation coupled with the deprotonations. This leads to a significant difference in frontier orbitals. In addition, the comparison of SOMO/SOMO−1 of **3-Ni-4H·DMSO** with LUMO/HOMO of **3-Ni-3H·0.5THF** and **3-Ni-2H·2H$_2$O** clearly shows the impact of deprotonation on the orbital distributions (Fig. 4 middle and bottom rows). The weights of the LUMOs/HOMOs on the deprotonated ligands significantly increased because of enhancements in the electron-accepting ability derived from the (semi)quinoidal structure (Fig. 2c). In particular, the HOMOs of the deprotonated crystals were considerably changed compared to the SOMO−1 of **3-Ni-4H·DMSO** (Fig. 4, bottom row). These results indicate that multiple oxidation and deprotonation efficiently modulate the d/π-electronic states of the nickel complexes in crystalline solids, which can impact functionalities such as transport properties; electrons migrate through drastically different orbitals before and after the oxidation-coupled deprotonation(s). The results suggest that this metal catecholdithiolene complex is a promising building block for pioneering novel electron–proton-coupled functionalities, where the d/π electronic states are significantly modulated by proton transfer on intermolecular H-bonds in the solid state by external stimuli.

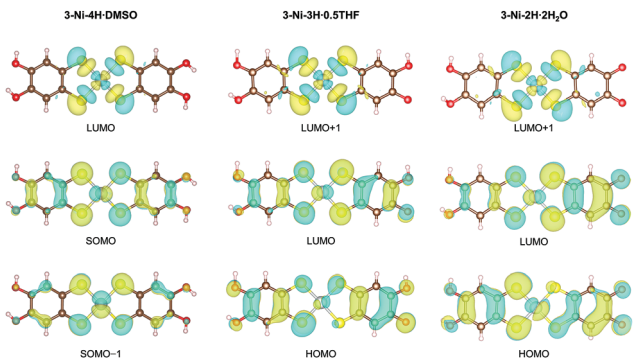

Fig. 4 Distributions of the frontier orbitals of the nickel complexes in **3-Ni-4H·DMSO**, **3-Ni-3H·0.5THF**, and **3-Ni-2H·2H$_2$O**. These figures were visualized by VESTA.[60]

Here, despite the moderate distance of the anionic [O–H···O]$^-$ H-bond ($d_{O\cdots O}$ = 2.590(3) Å) between the nickel complexes in **3-Ni-3H·0.5THF**, the C–O bond lengths of the hydroxy groups on the nickel complexes were similar (1.327(2) Å and 1.323(2) Å), resembling a symmetric H-bond with a proton in the center.[25,27,30] Thus, to determine the position of the proton in the short H-bond, differential Fourier maps based on the XRD measurements were drawn in Fig. S13a (ESI†). The electron density between the short H-bonds appears to be roughly distributed in the center of the oxygen atoms. However, the shape appears separated into two positions (Fig. S13a, ESI†). This demonstrates that the H-bond has a double-well potential, and the protons are disordered around two positions rather than the middle (0.5 : 0.5, Fig. S13a and c, ESI†), which shows that the electronic/molecular configuration is similar to that of **Ni-3H·0.5H$_2$O** (Fig. S7 and S8, ESI†). In addition, the position of the proton was not changed when the temperature varied from 293 to 130 K. However, the formation of such moderately short anionic H-bonds with disordered protons suggests that the nickel complex has a high potential to form H-bonds with disordered protons that are advantageous for d/π-electron–proton-coupled systems, where protons can be transferred by external stimuli in the solid state.

Possible mechanism of oxidation-coupled deprotonation on the nickel catecholdithiolene complex

Finally, we discuss the PCET route for the obtained crystals. As mentioned above, the three species of the nickel complexes undergoing PCET were obtained as different crystals with similar recrystallization conditions: non-deprotonated and non-oxidized complex, **[1−/4H]**; one-deprotonated and one-electron-oxidized complex, **[1−/3H]**; and two-deprotonated and one-electron-oxidized complex, **[2−/2H]** (Fig. 5). In addition to these species, crystals including neutral nickel complex without deprotonation (*i.e.*, non-deprotonation and one-electron oxidation), [Ni-H$_4$(catdt)$_2$]^0 (= **[0/4H]**, Fig. 5),[61] were also obtained by the recrystallization of **2-Ni** or the resulting green powder from **2-Ni** (see the Experimental section) with similar recrystallization conditions (from DMF/Et$_2$O or acetone/AcOH/hexane (**3-Ni-4H·DMF**: $(Ph_4P^+)_2[Ni\text{-}H_4(catdt)_2]^0(Br^-)_2\cdot DMF$, or **3-Ni-3,4H·solv**: $(Ph_4P^+)_2\{[Ni\text{-}H_3(catdt)_2]^-\}_2[Ni\text{-}H_4(catdt)_2]^0\cdot solv.$); the formulas and crystal structures are shown in the ESI,† Table S2 and Fig. S14–S16). However, reproducibility is yet to be fully confirmed. Considering these facts, we propose that the possible PCET process in this system is one-electron oxidation followed by one- or two-deprotonation, as shown in Fig. 5. We consider that the preceding one-electron oxidation promotes deprotonation(s) to gain an electrostatic potential, *i.e.*, Madelung energy, again with the complex being an anionic species. Here, the degree of deprotonation is controlled by the recrystallization conditions. The recrystallization using **2-Ni** from DMSO/H$_2$O or DMF/Et$_2$O yielded crystals with the non-deprotonated species **[1−/4H]** or **[0/4H]** (**3-Ni-4H·DMSO**

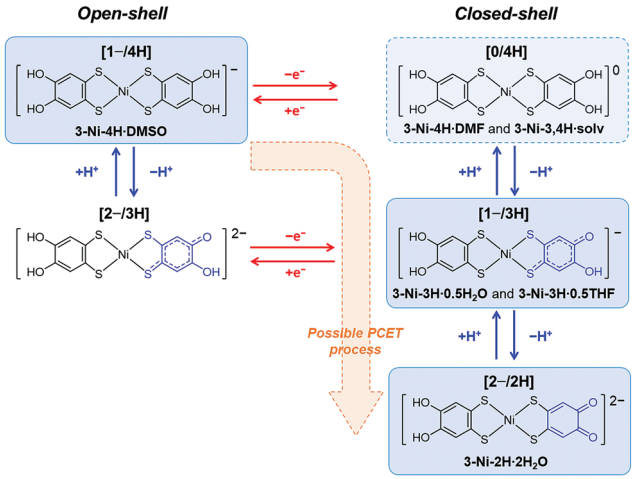

Fig. 5 Possible mechanism of oxidation-coupled deprotonation and chemical structure of the nickel complex in each state. Blue and red arrows show redox and protonation/deprotonation processes, respectively. **[1−/4H]**, **[0/4H]**, **[1−/3H]**, and **[2−/2H]** show monoanionic non-deprotonated, neutral non-deprotonated, monoanionic one-deprotonated, and dianionic two-deprotonated states of the nickel complex, respectively. The blue boxes with solid lines show the species obtained as crystals in this study. The blue box with a dashed line shows the species obtained as crystals with poor reproducibility presented in the ESI.†

or **3-Ni-4H·DMF**, respectively). Here the deprotonation is likely prevented by the existence of Br^- anions. In contrast, recrystallization using the green powder (prepared from **2-Ni**) yielded the crystals with **[1−/4H]**, **[1−/3H]**, or **[2−/2H]** depending on the recrystallization solvents (Fig. S1, ESI†). According to our previous work,[44] we consider that the green powder mainly consists of a 1 : 1 salt of Ph_4P cation and the nickel complex in **[1−/4H]** state containing the one-electron-oxidized species as minor components, which is supported by the ^{1}H NMR measurement (Fig. S17, ESI,† see also the Experimental section). During the recrystallization from DMSO/H_2O using the green powder, the non-oxidized species crystallizes without deprotonation as **3-Ni-4H·DMSO** (**[1−/4H]**), whereas the oxidized species, which would increase during the crystallization process to some extent, crystallize with deprotonation as **3-Ni-3H·0.5H_2O** (**[1−/3H]**) and **3-Ni-2H·2H_2O** (**[2−/2H]**). Such multiple deprotonations are because of the presence of water molecules with a proton-accepting ability. In this context, the presence of acetic acid will partially suppress the deprotonation, and thus the recrystallization from acetone/AcOH/hexane and THF/AcOH/hexane using the green powder yielded less-deprotonated crystals **3-Ni-3,4H·solv** (**[0/4H]** and **[1−/3H]**) and **3-Ni-3H·0.5THF** (**[1−/3H]**), respectively. The key to obtaining various PCET states **[1−/4H]**, **[0/4H]**, **[1−/3H]**, and **[2−/2H]** (Fig. 5) of the nickel complex as crystals is the redox-responsive deprotonation ability of catechol together with strong d/π conjugation and multi-redox activity of nickel dithiolene complexes, which are not present in π-conjugated systems.

Conclusions

In conclusion, we successfully synthesized new crystals with various oxidation/deprotonation states of the nickel catecholdithiolene complex. In the crystals, the nickel complexes formed various uncommon assembled structures (3D framework and 2D sheet) based on intermolecular H-bond formation. In particular, in **3-Ni-3H·0.5THF** and **3-Ni-3H·0.5H_2O**, the formation of anionic $[O–H\cdots O]^-$ H-bonds ($d_{O\cdots O}$ = ~2.59 Å) between the nickel complexes, which are advantageous for proton transfer in the solid state, was observed. ESR measurements revealed that the oxidation-coupled deprotonation caused changes in magnetic property, from paramagnetic to non-magnetic, in the nickel complexes. Thus, the magnetic properties and deprotonation states of the crystals were successfully controlled by recrystallization using PCET in solution processes. In addition, DFT calculations based on experimentally obtained structures suggest that the d/π frontier orbitals are significantly modulated in each crystal depending on the oxidation/deprotonation states. Furthermore, we successfully revealed the possible PCET route for the nickel catecholdithiolene complex through the crystallization of multiple PCET states (**[1−/4H]**, **[0/4H]**, **[1−/3H]**, and **[2−/2H]**, Fig. 5), which were realized by the characteristic features of the nickel dithiolene complex and catechol moiety. These findings demonstrate that the metal catecholdithiolene complexes are suitable candidates for exploring novel physical properties based on the coupling of d/π electrons and protons in solid states. In addition to the formation of anionic $[O–H\cdots O]^-$ H-bonds (low-barrier H-bonds) realized in these complexes, further modifications of the assembled structure will realize collective electronic properties in the solid state, which could pioneer a new field of functionalities based on d/π-electron–proton coupling.

Experimental section

Materials

Commercially available chemicals were used as received, without further purification. The chemicals used are listed below: acetic acid, hexane, diethyl ether, and *N*,*N*-dimethylformamide (guaranteed reagent grade, FUJIFILM Wako Pure Chemical Industries Ltd); methanol (super dehydrated grade, FUJIFILM Wako Pure Chemical Co., Ltd); tetrahydrofuran (super dehydrated, stabilizer free grade, FUJIFILM Wako Pure Chemical Co., Ltd); tetraphenylphosphonium bromide (Tokyo Chemical Industry Co., Ltd); and $Ni(OAc)_2{\cdot}4H_2O$ (guaranteed reagent grade, Kanto Chemical Co., Inc.).

Synthesis and crystallization

Brown plate crystals of the nickel catecholdithiolene complex, $(Ph_4P)_3[Ni\text{-}H_4(catdt)_2]Br_2$, **2-Ni**, were synthesized according to the previously reported method.[42] Subsequently, **2-Ni** was stirred at room temperature overnight under an argon atmosphere in a mixture of MeOH (4 mL) and H_2O (20 mL). The resulting green powder was filtered and washed with H_2O. The ^{1}H NMR (300 MHz) spectrum of the green powder was recorded on a JEOL JNM-AL300 spectrometer with DMSO-d_6 as a solvent and Me_4Si as an internal standard (Fig. S17, ESI†). According to our previous work on the $[Au(catdt)_2]^-$ complex,[44] the powder

obtained by stirring of $(Ph_4P)_3[Au\text{-}H_4(catdt)_2]Br_2$ in the MeOH/H_2O solution consisted of a 1 : 1 salt of Ph_4P^+ cation and the complex through the removal of Ph_4PBr. Thus, the green powder should also be composed of a 1 : 1 salt of Ph_4P^+ cation and the $[Ni(catdt)_2]^-$ complex. The ^1H NMR spectrum showed very weak signals from the nickel complexes, indicating that the complex in the green powder is mainly in the **[1−/4H]** state (NMR silent) containing the oxidized species **[0/4H]**, **[1−/3H]**, and/or **[2−/2H]** (NMR active) as minor species.

The green powder was then recrystallized from DMSO/H_2O under an argon atmosphere for several days to obtain green crystals of a DMSO-containing crystal and two H_2O-containing crystals with a large portion of amorphous solid: $(Ph_4P)[Ni\text{-}H_4(catdt)_2]\cdot$DMSO, **3-Ni-4H·DMSO** (dark green block); $(Ph_4P)[Ni\text{-}H_3(catdt)_2]\cdot 0.5H_2O$, **3-Ni-3H·0.5H$_2$O** (dark green needle); and $(Ph_4P)_2[Ni\text{-}H_2(catdt)_2]\cdot 2H_2O$, **3-Ni-2H·2H$_2$O** (brown plate). The crystals of **3-Ni-4H·DMSO** were also obtained and isolated by direct recrystallization of **2-Ni** from DMSO/H_2O without the significant amorphous compound. These **3-Ni-4H·DMSO** crystals prepared using the latter scheme were used for magnetic susceptibility measurements. Recrystallization of the green powder from THF/AcOH/hexane (*ca.* 10 : 1 : 30, AcOH = acetic acid) under an argon atmosphere for several days yielded the THF-containing crystal, $(Ph_4P)[Ni\text{-}H_3(catdt)_2]\cdot 0.5$THF, **3-Ni-3H·0.5THF**, in the form of dark green blocks without a significant amorphous compound. All the obtained materials contained good single crystals suitable for X-ray analysis, and only **3-Ni-4H·DMSO** was obtained in the order of 1 mg.

Single-crystal X-ray diffraction (XRD) measurements

X-ray diffraction (XRD) measurements for **3-Ni-4H·DMSO** and **3-Ni-3H·0.5H$_2$O** were performed on a Rigaku MercuryII CCD X-ray diffractometer (Mo K_α, λ = 0.71073 Å), and that for **3-Ni-2H·H$_2$O** was carried out on a Rigaku imaging plate system (synchrotron, λ = 0.99968 Å) at the BL-8A in the Photon Factory (PF), the High Energy Accelerator Research Organization (KEK), Japan. The initial structures were solved by direct methods (SHELXT version 2018/2) and refined using a full-matrix least-squares technique (SHELXL version 2018/3) using Olex2-1.3 (OlexSys).[62] Anisotropic thermal parameters were applied to non-hydrogen atoms. The positions of the hydrogen atoms on the hydroxy groups were refined, and the other hydrogen atoms were generated geometrically (C–H = 0.950 Å).

ESR measurements

X-band continuous wave ESR measurements were carried out using a Bruker EMXmicro spectrometer (9.435300–9.435596 GHz) at room temperature in air. Single crystals of **3-Ni-4H·DMSO**, **3-Ni-3H·0.5THF**, **3-Ni-3H·0.5H$_2$O**, and **3-Ni-2H·2H$_2$O** attached to a Teflon® rod in a quartz tube (ϕ = 5 mm) were used for the measurements. For **3-Ni-4H·DMSO**, the ESR spectra were collected by rotating the crystal around the *a*-axis of the crystal (0°: magnetic field perpendicular to the *c*-axis, and 90°: perpendicular to the *b*-axis). The ESR data were fitted by a differentiated Lorentz function, and the *g* value was estimated based on the fitting according to the following formula (eqn (1)).

$$I(B) = \frac{16 I'_m (B_0 - B)/(\Delta B_{pp}/2)}{\left[3 + \{(B_0 - B)/(\Delta B_{pp}/2)\}^2\right]^2} \quad (1)$$

where I_m', ΔB_{pp}, and B_0 show maximum intensity, peak-to-peak width, and resonance center, respectively.

Magnetic susceptibility measurements

Magnetic susceptibility measurements of polycrystalline **3-Ni-4H·DMSO** were performed using a Quantum Design SQUID magnetometer MPMS-XL in the temperature range of 2–300 K at a static magnetic field of 10 000 Oe. The magnetic susceptibility was corrected by considering the background data without the sample obtained separately, together with the diamagnetic contribution. The diamagnetic contribution of the compound was estimated to be -4.75×10^{-4} emu mol^{-1} from Pascal's constants.[63] The temperature dependence of the susceptibility was fitted by the Curie–Weiss law (eqn (2)).

$$\chi = \frac{C}{T - T_C} \quad (2)$$

where the χ, C, T, and T_C are magnetic susceptibility, Curie constant, absolute temperature, and Curie temperature, respectively. In addition, the *g* value was calculated from the result of the fitting using the Curie constant (Fig. S12, ESI†).

First-principles calculations

All DFT calculations were performed using OpenMX software (Ver. 3.9) based on optimized localized basis functions and pseudopotentials (PPs). The basis functions used were H6.0-s2p1, C6.0-s2p2d1, O6.0-s2p2d1, S7.0-s2p2d1f1, and Ni6.0H-s3p2d1 for hydrogen, carbon, oxygen, sulfur, and nickel, respectively; in the abbreviation of basis functions such as C6.0-s2p2d1, C is the atomic symbol, 6.0 represents the cutoff radius (bohr) in the generation by the confinement scheme, and s2p2d1 indicates the employment of two, two, and one optimized radial functions for the s-, p-, and d-orbitals, respectively. The radial functions were optimized by a variational optimization method.[64,65] As valence electrons in the PPs, we included 1s for hydrogen; 2s and 2p for carbon and oxygen; 3s and 3p for sulfur; 3s, 3p, 3d, and 4s for Ni. All the PPs and pseudo-atomic orbitals used in this study were taken from the database (2019) on the OpenMX website, which was benchmarked by the delta gauge method.[66] Realspace grid techniques were used for the numerical integrations and the solution of the Poisson equation using fast Fourier transform with an energy cutoff of 220 Ryd.[67] We used a generalized gradient approximation (GGA) proposed by Perdew, Burke, and Ernzerhof to the exchange–correlation functional.[68] An electronic temperature of 300 K was used to count the number of electrons by the Fermi–Dirac function for all the systems considered. For *k*-point sampling, we used a regular mesh of 1 × 1 × 1.

Molecular orbital calculations were carried out based on the crystal structure obtained by single-crystal XRD measurements.

For the calculations, three periodic hypothetical structures of **3-Ni-4H·DMSO**, **3-Ni-3H·0.5THF** and **3-Ni-2H·2H$_2$O** were used for these calculations, in which both Ph_4P^+ cations and crystal solvents were removed for **3-Ni-4H·DMSO** and **3-Ni-3H·0.5THF**, or only the Ph_4P^+ cations were removed for **3-Ni-4H·DMSO** and **3-Ni-2H·2H$_2$O**, where intermolecular H-bonds exist between the nickel complex and the crystal solvent. We adopted the structure refined by X-ray structural analysis with H atoms on the water molecules in **3-Ni-2H·2H$_2$O**; based on this, we confirmed that the atomic coordinates were almost the same between the cases with and without the H atoms on the water molecules (ESI† CIF for **3-Ni-2H·2H$_2$O**). In the calculation for **3-Ni-3H·0.5THF**, the occupancy of one of the disordered hydrogen atoms was assumed to be 1.00, and the other hydrogen atom was removed. Structural optimization was applied only to H atoms on the O atoms of the above-mentioned anionic H-bond in **3-Ni-3H·0.5THF**, and on the O atoms of water molecules in **3-Ni-2H·2H$_2$O**.

Conflicts of interest

There are no conflicts to declare.

Acknowledgements

This work was partially supported by JSPS Grants-in-Aid for Scientific Research (JP16H04010, JP17K18746, JP18H05225, JP19K05397, and JP20K15240), Grant-in-Aid for JSPS Fellows (JP20J12919), and MEXT Grants-in-Aid for Scientific Research on Innovative Areas ''Hydrogenomics'' (JP18H05516) and Transformative Research Area (A) ''Condensed Conjugation'' (JP20H05867). The synchrotron X-ray structural analysis was performed with the approval of the Photon Factory Program Advisory Committee (No. 2017S2-001 and 2020S2-001). We would like to thank Prof. Taisuke Ozaki and Dr. Mitsuaki Kawamura for the help with DFT calculations.

Notes and references

1 L. Pauling, *J. Am. Chem. Soc.*, 1931, **53**, 1367–1400.
2 T. Steiner, *Angew. Chem., Int. Ed.*, 2002, 48–76.
3 M. Bansal, *Curr. Sci.*, 2003, **85**, 1556–1563.
4 P. Li, Y. He, H. D. Arman, R. Krishna, H. Wang, L. Weng and B. Chen, *Chem. Commun.*, 2014, **50**, 13081–13084.
5 P. Li, Y. He, Y. Zhao, L. Weng, H. Wang, R. Krishna, H. Wu, W. Zhou, M. O'Keeffe, Y. Han and B. Chen, *Angew. Chem., Int. Ed.*, 2015, **54**, 574–577.
6 I. Hisaki, N. Q. Emilya Affendy and N. Tohnai, *CrystEngComm*, 2017, **19**, 4892–4898.
7 Y.-F. Han, Y.-X. Yuan and H.-B. Wang, *Molecules*, 2017, **22**, 266.
8 H. Wang, Z. Bao, H. Wu, R.-B. Lin, W. Zhou, T.-L. Hu, B. Li, J. C.-G. Zhao and B. Chen, *Chem. Commun.*, 2017, **53**, 11150–11153.
9 H. Wahl, D. A. Haynes and T. le Roex, *Cryst. Growth Des.*, 2017, **17**, 4377–4383.
10 M. Chang, A. Kobayashi, K. Nakajima, H.-C. Chang and M. Kato, *Inorg. Chem.*, 2011, **50**, 8308–8317.
11 M. Tadokoro and K. Nakasuji, *Coord. Chem. Rev.*, 2000, **198**, 205–218.
12 S. A. Baudron, N. Avarvari and P. Batail, *Inorg. Chem.*, 2005, **44**, 3380–3382.
13 M. Fourmigué and P. Batail, *Chem. Rev.*, 2004, **104**, 5379–5418.
14 M. Hayashi, K. Otsubo, T. Kato, K. Sugimoto, A. Fujiwara and H. Kitagawa, *Chem. Commun.*, 2015, **51**, 15796–15799.
15 M. Hayashi, K. Otsubo, M. Maesato, T. Komatsu, K. Sugimoto, A. Fujiwara and H. Kitagawa, *Inorg. Chem.*, 2016, **55**, 13027–13034.
16 T. Higashino, A. Ueda, J. Yoshida and H. Mori, *Chem. Commun.*, 2017, **53**, 3426–3429.
17 Y. Sunairi, A. Ueda, J. Yoshida, K. Suzuki and H. Mori, *J. Phys. Chem. C*, 2018, **122**, 11623–11632.
18 S. Cai, H. Shi, Z. Zhang, X. Wang, H. Ma, N. Gan, Q. Wu, Z. Cheng, K. Ling, M. Gu, C. Ma, L. Gu, Z. An and W. Huang, *Angew. Chem., Int. Ed.*, 2018, **57**, 4005–4009.
19 T. Akutagawa, S. Takeda, T. Hasegawa and T. Nakamura, *J. Am. Chem. Soc.*, 2004, **126**, 291–294.
20 S. Horiuchi, F. Ishii, R. Kumai, Y. Okimoto, H. Tachibana, N. Nagaosa and Y. Tokura, *Nat. Mater.*, 2005, **4**, 163–166.
21 M. Tadokoro, T. Inoue, S. Tamaki, K. Fujii, K. Isogai, H. Nakazawa, S. Takeda, K. Isobe, N. Koga, A. Ichimura and K. Nakasuji, *Angew. Chem., Int. Ed.*, 2007, **46**, 5938–5942.
22 S. Horiuchi, Y. Tokunaga, G. Giovannetti, S. Picozzi, H. Itoh, R. Shimano, R. Kumai and Y. Tokura, *Nature*, 2010, **463**, 789–792.
23 D. R. Weinberg, C. J. Gagliardi, J. F. Hull, C. F. Murphy, C. A. Kent, B. C. Westlake, A. Paul, D. H. Ess, D. G. McCafferty and T. J. Meyer, *Chem. Rev.*, 2012, **112**, 4016–4093.
24 S. C. Lee, A. Ueda, H. Kamo, K. Takahashi, M. Uruichi, K. Yamamoto, K. Yakushi, A. Nakao, R. Kumai, K. Kobayashi, H. Nakao, Y. Murakami and H. Mori, *Chem. Commun.*, 2012, **48**, 8673.
25 T. Isono, H. Kamo, A. Ueda, K. Takahashi, A. Nakao, R. Kumai, H. Nakao, K. Kobayashi, Y. Murakami and H. Mori, *Nat. Commun.*, 2013, **4**, 1344.
26 T. Isono, H. Kamo, A. Ueda, K. Takahashi, M. Kimata, H. Tajima, S. Tsuchiya, T. Terashima, S. Uji and H. Mori, *Phys. Rev. Lett.*, 2014, **112**, 177201.
27 J. Yoshida, A. Ueda, A. Nakao, R. Kumai, H. Nakao, Y. Murakami and H. Mori, *Chem. Commun.*, 2014, **50**, 15557–15560.
28 J. Yoshida, A. Ueda, R. Kumai, Y. Murakami and H. Mori, *CrystEngComm*, 2017, **19**, 367–375.
29 M. Tadokoro, H. Hosoda, T. Inoue, A. Murayama, K. Noguchi, A. Iioka, R. Nishimura, M. Itoh, T. Sugaya, H. Kamebuchi and M. Haga, *Inorg. Chem.*, 2017, **56**, 8513–8526.
30 A. Ueda, S. Yamada, T. Isono, H. Kamo, A. Nakao, R. Kumai, H. Nakao, Y. Murakami, K. Yamamoto, Y. Nishio and H. Mori, *J. Am. Chem. Soc.*, 2014, **136**, 12184–12192.

31 A. Ueda, *Bull. Chem. Soc. Jpn.*, 2017, **90**, 1181–1188.
32 A. Ueda, K. Kishimoto, Y. Sunairi, J. Yoshida, H. Yamakawa, T. Miyamoto, T. Terashige, H. Okamoto and H. Mori, *J. Phys. Soc. Jpn.*, 2019, **88**, 034710.
33 A. Ueda, K. Kishimoto, T. Isono, S. Yamada, H. Kamo, K. Kobayashi, R. Kumai, Y. Murakami, J. Gouchi, Y. Uwatoko, Y. Nishio and H. Mori, *RSC Adv.*, 2019, **9**, 18353–18358.
34 Y. Kobayashi, K. Hirata, S. N. Hood, H. Yang, A. Walsh, Y. Matsushita and K. Ishioka, *Chem. Sci.*, 2020, **11**, 11699–11704.
35 S. Yokomori, S. Dekura, T. Fujino, M. Kawamura, T. Ozaki and H. Mori, *J. Mater. Chem. C*, 2020, **8**, 14939–14947.
36 T. Mitani, G. Saito and H. Urayama, *Phys. Rev. Lett.*, 1988, **60**, 2299–2302.
37 M. Kubinyi and G. Keresztury, *Spectrochim. Acta, Part A*, 1989, **45**, 421–429.
38 K. Nakasuji, K. Sugiura, T. Kitagawa, J. Toyoda, H. Okamoto, K. Okaniwa, T. Mitani, H. Yamamoto and I. Murata, *J. Am. Chem. Soc.*, 1991, **113**, 1862–1864.
39 M. Shimozawa, K. Hashimoto, A. Ueda, Y. Suzuki, K. Sugii, S. Yamada, Y. Imai, R. Kobayashi, K. Itoh, S. Iguchi, M. Naka, S. Ishihara, H. Mori, T. Sasaki and M. Yamashita, *Nat. Commun.*, 2017, **8**, 1821.
40 H. Kamo, A. Ueda, T. Isono, K. Takahashi and H. Mori, *Tetrahedron Lett.*, 2012, **53**, 4385–4388.
41 S. Horiuchi, R. Kumai and Y. Tokura, *J. Am. Chem. Soc.*, 2005, **127**, 5010–5011.
42 D. Coucouvanis, A. R. Paital, Q. Zhang, N. Lehnert, R. Ahlrichs, K. Fink, D. Fenske, A. K. Powell and Y. Lan, *Inorg. Chem.*, 2009, **48**, 8830–8844.
43 Y. Le Gal, T. Roisnel, P. Auban-Senzier, T. Guizouarn and D. Lorcy, *Inorg. Chem.*, 2014, **53**, 8755–8761.
44 S. Yokomori, A. Ueda, T. Higashino, R. Kumai, Y. Murakami and H. Mori, *CrystEngComm*, 2019, **21**, 2940–2948.
45 H. Hachem, N. Bellec, M. Fourmigué and D. Lorcy, *Dalton Trans.*, 2020, **49**, 6056–6064.
46 Y. Kimura, Y. Toshida, M. Maesato and H. Kitagawa, *Chem. Lett.*, 2021, **50**, 439–441.
47 N. Robertson and L. Cronin, *Coord. Chem. Rev.*, 2002, **227**, 93–127.
48 R. Kato, *Chem. Rev.*, 2004, **104**, 5319–5346.
49 A. Kobayashi, E. Fujiwara and H. Kobayashi, *Chem. Rev.*, 2004, **104**, 5243–5264.
50 W.-Y. Guo, Z.-H. Peng, C.-G. Wang and Y.-H. Zhou, *J. Coord. Chem.*, 2006, **59**, 1213–1223.
51 D. Lorcy, N. Bellec, M. Fourmigué and N. Avarvari, *Coord. Chem. Rev.*, 2009, **253**, 1398–1438.
52 R. Kato, *Bull. Chem. Soc. Jpn.*, 2014, **87**, 355–374.
53 F. Pop and N. Avarvari, *Coord. Chem. Rev.*, 2017, **346**, 20–31.
54 H. Hachem, O. Jeannin, M. Fourmigué, F. Barrière and D. Lorcy, *CrystEngComm*, 2020, **22**, 3579–3587.
55 T. Kusamoto, H. M. Yamamoto, N. Tajima, Y. Oshima, S. Yamashita and R. Kato, *Inorg. Chem.*, 2012, **51**, 11645–11654.
56 T. Kusamoto, H. M. Yamamoto, N. Tajima, Y. Oshima, S. Yamashita and R. Kato, *Inorg. Chem.*, 2013, **52**, 4759–4761.
57 A. Filatre-Furcate, N. Bellec, O. Jeannin, P. Auban-Senzier, M. Fourmigué, A. Vacher and D. Lorcy, *Inorg. Chem.*, 2014, **53**, 8681–8690.
58 H. Hachem, H. Cui, T. Tsumuraya, R. Kato, O. Jeannin, M. Fourmigué and D. Lorcy, *J. Mater. Chem. C*, 2020, **8**, 11581–11592.
59 A. Abhervé, N. Mroweh, T. Cauchy, F. Pop, H. Cui, R. Kato, N. Vanthuyne, P. Alemany, E. Canadell and N. Avarvari, *J. Mater. Chem. C*, 2021, **9**, 4119–4140.
60 K. Momma and F. Izumi, *J. Appl. Crystallogr.*, 2011, **44**, 1272–1276.
61 The compositions of the crystals including neutral nickel complex, **3-Ni-4H·DMF** and **3-Ni-3,4H·solv**, were determined by single-crystal X-ray structural analyses as $(Ph_4P)_2[Ni\text{-}H_4(catdt)_2]Br_2\cdot DMF$ and $(Ph_4P)_2[Ni\text{-}H_3(catdt)_2]_2[Ni\text{-}H_4(catdt)_2]\cdot solv.$, respectively. For 3-Ni-4H·DMF, because Ph_4P and Br are monocation and monoanion in the crystal, respectively, the nickel complex is in a neutral state based on the charge neutrality of a crystal. For **3-Ni-3,4H·solv**, the crystal consisted of two equivalents of one-molecule independent Ph_4P, two equivalents of one-molecule independent nickel complex, and one equivalent of half-molecule independent nickel complex. Thus, the half-molecule independent nickel complex should be in a neutral state. In addition, it is confirmed that the neutral nickel complexes in the crystals were not deprotonated from the comparison of the C–O bond lengths. Hence, we concluded that these crystals contain a neutral non-deprotonated nickel complex.
62 O. V. Dolomanov, L. J. Bourhis, R. J. Gildea, J. A. K. Howard and H. Puschmann, *J. Appl. Crystallogr.*, 2009, **42**, 339–341.
63 G. A. Bain and J. F. Berry, *J. Chem. Educ.*, 2008, **85**, 532.
64 T. Ozaki, *Phys. Rev. B: Condens. Matter Mater. Phys.*, 2003, **67**, 155108.
65 T. Ozaki and H. Kino, *Phys. Rev. B: Condens. Matter Mater. Phys.*, 2004, **69**, 195113.
66 K. Lejaeghere, G. Bihlmayer, T. Björkman, P. Blaha, S. Blügel, V. Blum, D. Caliste, I. E. Castelli, S. J. Clark, A. Dal Corso, S. de Gironcoli, T. Deutsch, J. K. Dewhurst, I. Di Marco, C. Draxl, M. Dułak, O. Eriksson, J. A. Flores-Livas, K. F. Garrity, L. Genovese, P. Giannozzi, M. Giantomassi, S. Goedecker, X. Gonze, O. Grånäs, E. K. U. Gross, A. Gulans, F. Gygi, D. R. Hamann, P. J. Hasnip, N. A. W. Holzwarth, D. Iuşan, D. B. Jochym, F. Jollet, D. Jones, G. Kresse, K. Koepernik, E. Küçükbenli, Y. O. Kvashnin, I. L. M. Locht, S. Lubeck, M. Marsman, N. Marzari, U. Nitzsche, L. Nordström, T. Ozaki, L. Paulatto, C. J. Pickard, W. Poelmans, M. I. J. Probert, K. Refson, M. Richter, G.-M. Rignanese, S. Saha, M. Scheffler, M. Schlipf, K. Schwarz, S. Sharma, F. Tavazza, P. Thunström, A. Tkatchenko, M. Torrent, D. Vanderbilt, M. J. van Setten, V. Van Speybroeck, J. M. Wills, J. R. Yates, G.-X. Zhang and S. Cottenier, *Science*, 2016, **351**, aad3000.
67 T. Ozaki and H. Kino, *Phys. Rev. B: Condens. Matter Mater. Phys.*, 2005, **72**, 045121.
68 J. P. Perdew, K. Burke and M. Ernzerhof, *Phys. Rev. Lett.*, 1996, **77**, 3865–3868.

